# Understanding the Synthetic Pathway of a Single-Phase Quaternary Semiconductor Using Surface-Enhanced Raman Scattering: A Case of Wurtzite Cu₂ZnSnS₄ Nanoparticles

Joel Ming Rui Tan,[†,‡,§,∥] Yih Hong Lee,[§] Srikanth Pedireddy,[§] Tom Baikie,[‡] Xing Yi Ling,*,[§] and Lydia Helena Wong*,[‡,∥]

[†]Interdisciplinary Graduate School, [‡]Energy Research Institute, [§]Division of Chemistry and Biological Chemistry, School of Physical and Mathematical Sciences, and [∥]School of Material Science and Engineering, Nanyang Technological University, Singapore 639798

S *Supporting Information*
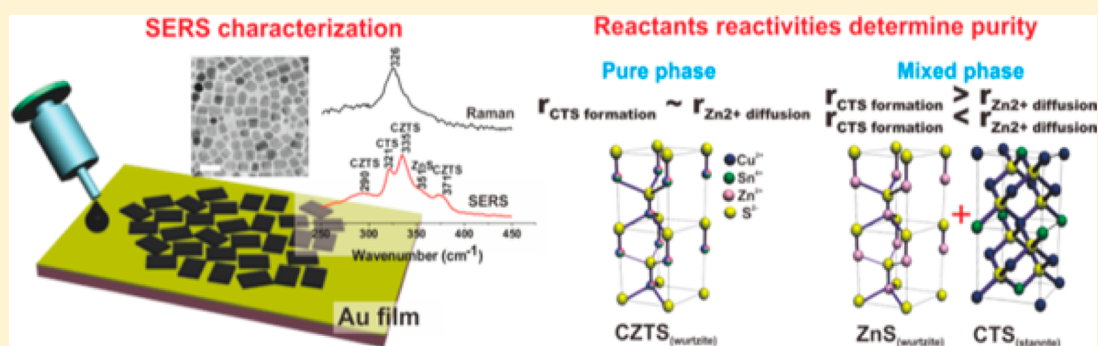
ABSTRACT: Single-phase Cu₂ZnSnS₄ (CZTS) is an essential prerequisite toward a high-efficiency thin-film solar cell device. Herein, the selective phase formation of single-phase CZTS nanoparticles by ligand control is reported. Surface-enhanced Raman scattering (SERS) spectroscopy is demonstrated for the first time as a characterization tool for nanoparticles to differentiate the mixed compositional phase (e.g., CZTS, CTS, and ZnS), which cannot be distinguished by X-ray diffraction. Due to the superior selectivity and sensitivity of SERS, the growth mechanism of CZTS nanoparticle formation by hot injection is revealed to involve three growth steps. First, it starts with nucleation of $Cu_{2-x}S$ nanoparticles, followed by diffusion of Sn^{4+} into $Cu_{2-x}S$ nanoparticles to form the Cu_3SnS_4 (CTS) phase and diffusion of Zn^{2+} into CTS nanoparticles to form the CZTS phase. In addition, it is revealed that single-phase CZTS nanoparticles can be obtained via balancing the rate of CTS phase formation and diffusion of Zn^{2+} into the CTS phase. We demonstrate that this balance can be achieved by 1 mL of thiol with $Cu(OAc)_2$, $Sn(OAc)_4$, and $Zn(acac)_2$ metal salts to synthesize the CZTS phase without the presence of a detectable binary/ternary phase with SERS.

■ INTRODUCTION

Cu₂ZnSnS₄ (CZTS), a quaternary chalcogenide p-type semiconductor, is actively studied as a photovoltaic material due to its high absorption coefficient ($\sim 10^4$ cm⁻¹), optimal direct band energy of $\sim 1.0-1.5$ eV, as well as being composed of naturally abundant and nontoxic elements.[1−3] The theoretical power conversion efficiency of a CZTS solar cell is 29.4%; however the best reported experimental data to date, achieved by solution method, is only 12.6%.[4,5] This huge gap between the theoretical and experimental power conversion efficiencies can be attributed to a number of factors, such as lack of stoichiometric control, complicated nature of the bulk and surface defects, as well as difficulty in producing single-phase CZTS without a secondary phase.[6]

Recently, wet-chemical syntheses of CZTS nanoparticles have attracted much attention due to their ease of scalability and versatility of such single-phased nanoparticles to be used as inks in a wide range of printing techniques, such as roll-to-roll, screen printing, and spray pyrolysis.[7−13] One of the challenges

in the synthesis of CZTS nanoparticles is the tendency to form binary (i.e., copper sulfide, zinc sulfide, tin sulfide) and ternary sulfides (copper−tin−sulfide, CTS).[14,15] Among these secondary phases, conducting phases (CTS and Cu₂S) are most detrimental to the electrical performance of CZTS as they lead to short-circuitry of the photovoltaic device and quenching of electron−hole pairs.[16,17] Consequently, the ability to prepare compositionally pure CZTS-phase nanoparticles has become the top priority in increasing the efficiency of CZTS nanoparticle-based solar cells. The fusing of pure-phase nanoparticles to form a bulk thin film avoids random nucleation faced by other solution process methods.[18] It is therefore important to understand the growth mechanism and synthetic chemistry of CZTS nanoparticle formation to achieve a reproducible synthetic route for single-phase CZTS nanoparticles. Investigations on the synthesis of CZTS nanoparticles

can be collectively classified as studying the influence of capping agents,[19] thiol source, and metal salt precursors on the resulting CZTS crystal structure[7,13,20,21] (e.g., kesterite (k), wurtzite (w)), morphology,[22−24] and elemental composition of CZTS nanoparticles.[25] While the influence of metal salt precursors on chalcopyrite compositional phase (e.g CuS, $Cu_{1.8}S$) formation has been reported before,[26] there is no report on the influence of the metal salt precursors on the CZTS compositional phase (e.g CZTS, CTS) formation to date.

Currently, X-ray diffraction (XRD) and Raman spectroscopy are the two primary techniques used to characterize the crystal structure and compositional purity of CZTS nanoparticles. However, there are inherent complexities related to the use of these techniques in characterizing the compositional purity of CZTS nanoparticles.[24] XRD is unable to accurately distinguish the presence of CTS (stannite/orthorhombic) and CZTS (wurtzite/kesterite) phases due to overlapping diffraction peaks.[12] On the other hand in Raman spectroscopy, the characteristic vibrational modes of bulk CZTS (338 cm^{-1}), Cu_3SnS_4 (318 cm^{-1}), Cu_2SnS_3 (298 cm^{-1}), and $Cu_{2-x}S$ (269, 301, and 470 cm^{-1}) can be resolved reasonably well, and coexisting phases can be differentiated from each other.[12,27,28] However, the sensitivity of Raman spectroscopy is poor as a result of the small Raman scattering cross sections of these nanoparticles.[29] This small Raman scattering cross section however can be increased by using surface-enhanced Raman scattering (SERS) spectroscopy.[30] In SERS, noble metal nanoparticles (Au and Ag) are used because of the ability of the localized surface plamons of these metal nanoparticles to concentrate incident light into subwavelength volumes.[31,32] As a result, local electromagnetic fields in the vicinity of the nanoparticles are strongly enhanced.[33,34] These intensified fields in turn produce hot spots around the metal nanoparticles that lead to large SERS enhancement factors.

Herein, we demonstrate the use of SERS spectroscopy as a sensitive characterization technique to fully identify and differentiate the Raman peaks of various compositional phases present in the synthesized CZTS nanoparticles. The use of SERS overcomes the problem of small Raman scattering cross sections for CZTS nanoparticles. With this capability, we aim to understand the formation mechanism of CZTS nanoparticles by controlling the coordinating strengths of the chelating ligands of metal precursors. We employ two organic ligands, that is, acetylacetonate (acac) and acetate (OAc), of different binding strengths. The effect of having a stronger ligand on an individual element (Cu^{2+}, Zn^{2+}, and Sn^{4+}) on the CZTS nanoparticle formation is examined, and the vital reaction steps to achieve pure CZTS-phase nanoparticles is identified. On the basis of our findings, we establish an optimal set of parameters to synthesize compositionally pure wurtzite-phase nanoplate-like CZTS nanoparticles in high monodispersity. The synthetic pathway revealed in this work may also be extended to produce single-phase $Cu_2(M)SnS_4$ (where M = Ni, Co, Fe, Mn) that has recently been reported with possible applications in optoelectronic, magnetic, and electronic devices.[35]

■ RESULTS AND DISCUSSION

As shown in Figure 1a, nanoplates are obtained in high monodispersity, with an average size of 10 ± 3 nm. The as-synthesized CZTS nanoparticles are drop-casted on a Si/SiO$_x$ substrate to form a thick film for XRD (Figure 1b) and normal Raman measurements (Figure 1g). The XRD patterns of ZnS
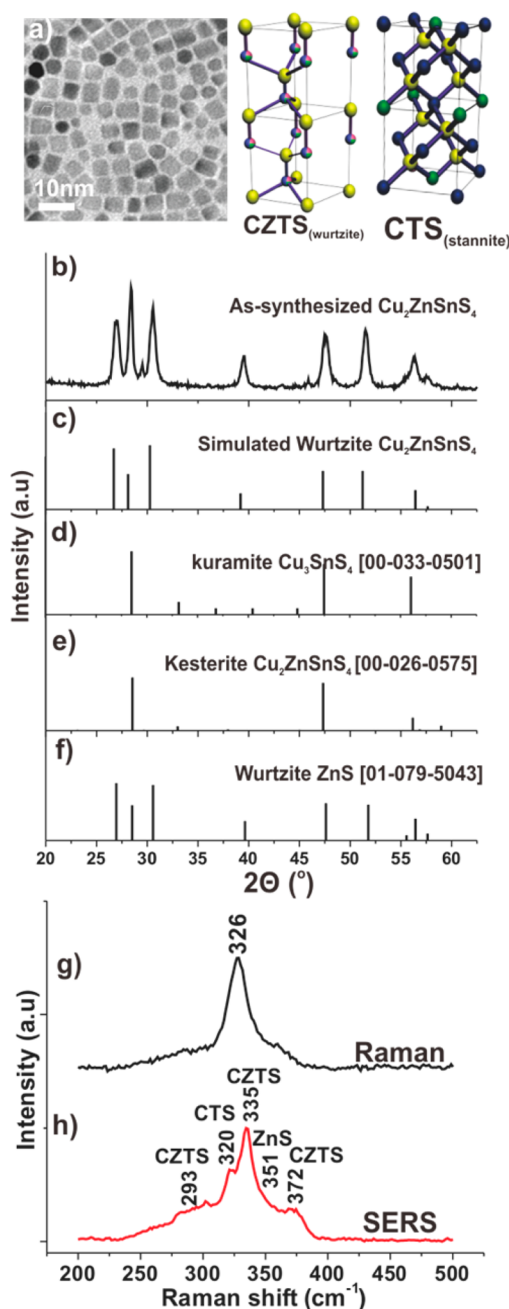

Figure 1. (a) TEM images of as-synthesized CZTS nanoparticles. Powder XRD patterns of (b) as-synthesized CZTS nanoparticles, (c) simulated CZTS, (d) kuramite CTS, (e) kesterite CZTS, and (f) wurtzite ZnS. (g) Raman and (h) SERS spectra of as-synthesized CZTS nanoparticles containing multiple phases. The inset shows the nanoparticle obtained from Sn-acac, and 1 mL of DDT was used for the Raman and SERS spectroscopy.

(w), CTS (k), CZTS (k), and CZTS (w) (Figure 1c−f) reveal that, due to the overlapping diffraction peaks of the possible phases, we are unable to determine the purity and identity of the compositional phases present using XRD. In addition, the normal Raman scattering spectrum of the as-synthesized CZTS nanoparticles is shown in Figure 1g, where only an ambiguous peak at 326 cm^{-1} is detected, possibly arising from a mixture of phases (CZTS, CTS). On the other hand, when SERS measurements (Figure 1h) are carried out on a thin film (∼10 ± 5 nm) of the same CZTS nanoparticles drop-casted on
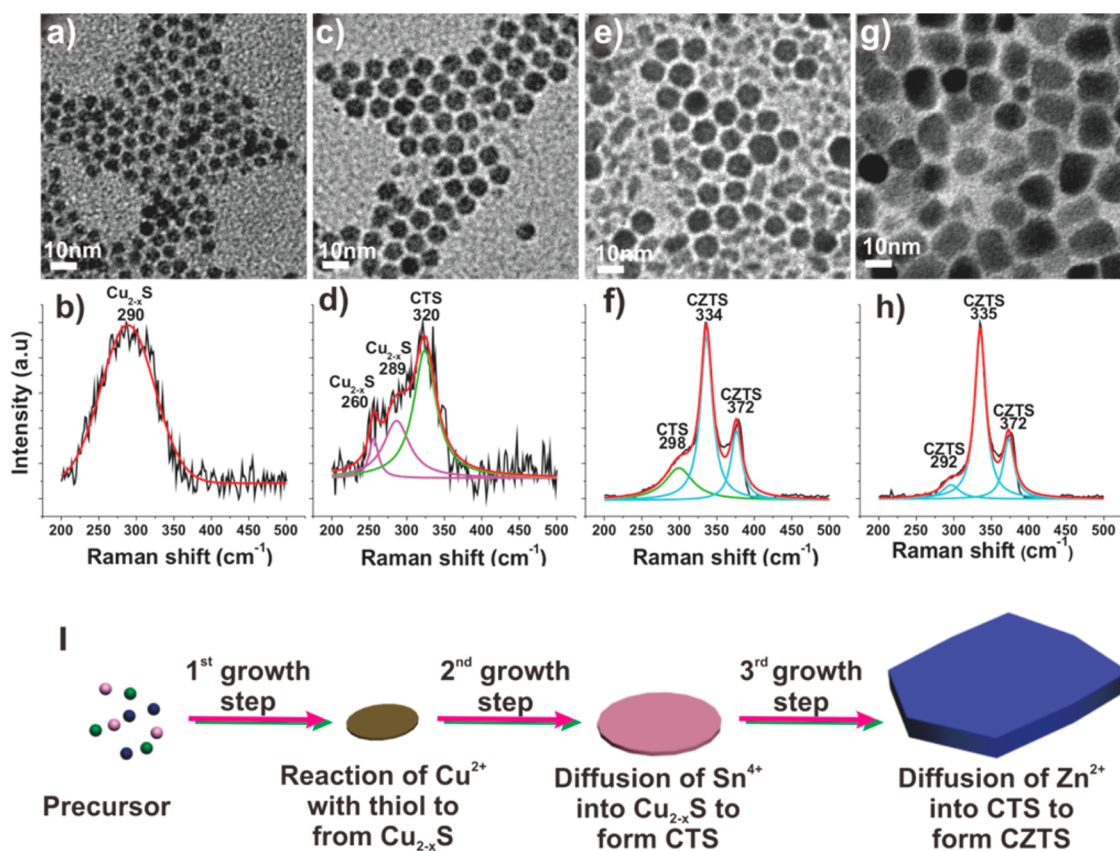
Figure 2. CZTS nanoparticles extracted at different reaction times at 240 °C. (a) TEM images and (b) SERS spectra at 2 min, (c) TEM images and (d) SERS spectra at 8 min, (e) TEM images and (f) SERS spectra at 12 min, and (g) TEM images and (h) SERS spectra at 90 min. (i) Pictorial representation of the three step growth process for the formation of CZTS nanoparticles.

a 50 nm thick gold film (Figure S1, Supporting Information), five distinct peaks could be observed, which can be unambiguously assigned to CZTS (293, 335, and 372 cm^{-1}), CTS (320 cm^{-1}), and ZnS phases (351 cm^{-1}).[12,28,36] The preliminary characterization of the as-synthesized CZTS nanoparticles highlights the superiority of SERS over conventional Raman spectroscopy and XRD in detecting the presence of both CZTS and other binary/ternary phases in the CZTS nanoparticles. From here onward, SERS will be used as the main characterization tool to identify the phases in the synthesized CZTS nanoparticles in the subsequent experiments. XRD coupled with Rietveld refinements will be used to determine the crystal structure of the nanoparticles based on the phases identified from SERS.

Establishing the Growth Mechanism of CZTS Nanoparticles. To thoroughly identify the individual growth steps involved in CZTS nanoparticles formation that could not be achieved with XRD, we carry out the reaction reported by Liao et al.[37] with modifications, and monitor the reaction progress during the formation of CZTS nanoparticles by SERS. Aliquots are withdrawn from the reaction mixture at regular intervals, and the corresponding morphology and compositional phase are examined by transmission electron microscopy (TEM) and SERS, respectively. After 2 min of reaction, a broad peak at ~290 cm^{-1} corresponding to the Cu$_{2-x}$S phase (Figure 2b) is observed when the solution turns black.[32] As shown in the TEM image (Figure 2a), the formation of CZTS nanoparticles is observed to begin with the formation of Cu$_{2-x}$S nuclei (~4 nm). After 8 min of reaction, three Raman peaks are observed at 260 and 289 cm^{-1} corresponding to the Cu$_{2-x}$S phase and at

320 cm^{-1} corresponding to the CTS phase (Figure 2d).[38,39] The presence of the CTS phase indicates the diffusion of Sn^{4+} into Cu$_{2-x}$S nanoparticles that also results in the growth of Cu$_{2-x}$S/CTS nanoparticles to ~8 nm (Figure 2c). After 12 min of reaction, three Raman peaks (Figure 2f) are observed at 298 cm^{-1} (CTS phase) and at 334 and 372 cm^{-1} (CZTS phase). The presence of the CZTS phase indicates the diffusion of Zn^{2+} into the CTS phase. From the TEM images (Figure 2e), smaller nanoparticles of ~2−4 nm are observed along with larger nanoparticles of ~10 nm. Finally, after 90 min of reaction, three Raman peaks (Figure 2h) at 292, 335, and 372 cm^{-1} corresponding to the CZTS phase are observed along with an increase in nanoparticles to ~14 nm (Figure 2g). This finding of CZTS nanoparticles proceeding from Cu$_{2-x}$S nuclei complements the experimental observation reported by recent studies.[23,37,40] In addition, we have demonstrated the growth of the CZTS phase is originated via the CTS phase, which has not been identified until now.[40]

From this growth study, three growth steps have been proposed. The first step involved the nucleation of Cu$_{2-x}$S nanoparticles, followed by the diffusion of Sn^{4+} into Cu$_{2-x}$S nanoparticles to form CTS nanoparticles and lastly the diffusion of Zn^{2+} into CTS nanoparticles to form CZTS nanoparticles. The sequence of phase transformation starting from diffusion of Sn^{4+} rather than Zn^{2+} cations into Cu$_{2-x}$S nanoparticles is agreeable to reports on the unfavorable formation of the Cu−Zn−S ternary system but as heterogeneous Cu$_{2-x}$S−ZnS nanoparticles instead.[41,42] In addition, the observations of smaller nanoparticles along with larger nanoparticles (Figure 2e) during the growth of CZTS

nanoparticles suggest the growth to proceed via Ostwald ripening. These finding highlights the specificity of CZTS nanoparticle formation thus realizing the need to identify the purity-determining growth step. To study the importance of growth rate at each step, a stronger binding ligand will be used to reduce the reactivity of the cations at each growth step (Figure 2i). An OAc−metal complex is less stable than an acac−metal complex because the former forms a less stable four-membered ring with the metal cation as compared to a more stable six-membered ring formed by the metal−acac complex.[43]

Understanding Ligand Effect on CZTS Nanoparticle Formation. Systematic study on the effect of a stronger binding metal−ligand complex on CZTS nanoparticle synthesis is carried out (Table 1). OAc reaction (no acac ligand used)

Table 1. Four Different Reaction Setups Are Carried Out to Study the Effect of Cation Reactivity on CZTS Phase Formation[a]

Reaction Setup	Metal precursor		
	Cu salt:	Sn salt:	Zn salt:
I Oac	$Cu(OAc)_2$	$Sn(OAc)_4$	$Zn(OAc)_2$
II Cu-acac	$Cu(acac)_2$	$Sn(OAc)_4$	$Zn(OAc)_2$
III Sn-acac	$Cu(OAc)_2$	$Sn(acac)_2Cl_2$	$Zn(OAc)_2$
IV Zn-acac	$Cu(OAc)_2$	$Sn(OAc)_4$	$Zn(acac)_2$

Ligands: acetate ions (OAc), acetylacetonate ions (acac)

[a](I) Oac: all cations are binded to acetate ligands; (II) Cu−acac: acetate ligands on Cu cations are substituted with acetylacetonate ligands; (III) Sn−acac: acetate ligands on Sn cations are substituted with acetylacetonate ligands; (IV) Zn−acac: acetate ligands on Zn cations are substituted with acetylacetonate ligands.

serves as a control experiment, while the Cu−acac reaction ($Cu(acac)_2$ as Cu^{2+} metal salt) demonstrates the effect of reducing Cu^{2+} reactivity in $Cu_{2-x}S$ phase growth, the Sn−acac reaction ($Sn(acac)_2Cl_2$ as Sn^{4+} metal salt) shows the effects of reducing Sn^{4+} reactivity during the diffusion of Sn^{4+} into $Cu_{2-x}S$ to form the CTS phase, and lastly, the Zn−acac reaction ($Zn(acac)_2$ as Zn^{2+} metal salt) shows the effect of reducing Zn^{2+} reactivity during Zn^{2+} diffusion into the CTS phase to form the CZTS phase. SERS is used to characterize the synthesized nanoparticles from the different metal salt combinations with the amount of 1-dodecanethiol (DDT) kept constant at 1 mL to fix the amount of sulfur source available in all the reactions. First, the control experiment with all acetate−metal complexes (OAc reaction) is carried out. The SERS spectrum (Figure 3b) of nanoparticles obtained from the OAc reaction shows three peaks at ∼292, 336, and 372 cm^{-1} indicating compositionally pure CZTS phase. In addition, the morphology of CZTS nanoparticles obtained (Figure 3a) show bricklike morphology with a size distribution of 9 ± 3 nm and pure wurtzite (CZTS) crystal structure (Figure S2, Supporting Information). Next, a stronger binding ligand−copper complex ($Cu(acac)_2$) is used. The SERS spectrum (Figure 3d) of
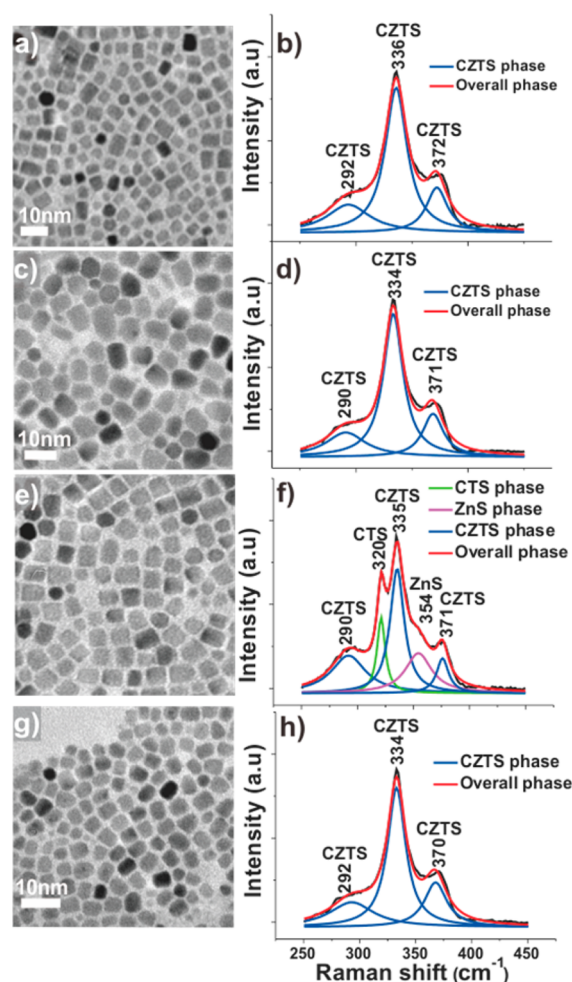

Figure 3. TEM images (left column) and SERS spectra (right column) of CZTS nanoparticles synthesized using different reaction setups at a 1 mL amount of DDT. (a, b) setup I, Oac; (c, d) setup II, Cu−acac; (e, f) setup III, Sn−acac; (g, h) setup IV, Zn−acac.

nanoparticles obtained from the Cu−acac reaction shows three peaks at ∼290, 334, and 371 cm^{-1} indicating compositionally pure CZTS phase. The nanoparticles obtained from Cu−acac (Figure 3c) shows random oval-like morphology with a size distribution of 9 ± 4 nm and pure wurtzite (CZTS) crystal structure (Figure S3, Supporting Information). The lack of consistent morphology as compared to OAc (Figure 3a) suggests nonhomogenous growth of CZTS nanoparticles. This implies that reduction of Cu^{2+} reactivity inhibits homogeneous growth of nanoparticles but does not affect the phase transformation during CZTS nanoparticle formation. There is no difference in compositional phase purity between the OAc reaction (Figure 3b) and the Cu−acac reaction (Figure 3d) because of the much higher affinity of Cu^{2+} over Sn^{4+} and Zn^{2+} to the sulfur source (DDT) despite having acac as the chelating ligand.[44] This leads to the rapid formation of the $Cu_{2-x}S$ phase, which has been shown earlier to be essential for the formation of CZTS nanoparticles. During the reaction, Cu^{2+} is readily reduced to Cu^+ by DDT due to its low reduction potential of +0.159 V versus NHE.[45−47] The higher affinity of Cu^+ to DDT arises from the better soft−soft compatibility between these two ionic species as compared to Sn^{4+} and Zn^{2+} with DDT.[48,49] The ranking of the cations can be ranked as $Cu^+ > Cu^{2+}$ and $Zn^{2+} > Sn^{4+}$.[35,36] Consequently, the influence of acac on Cu^{2+}

reactivity shows little effect on the formation of CZTS nanoparticles due to the high affinity of Cu^{2+} for thiol.

Next, a stronger binding ligand−tin complex ($Sn(acac)_2Cl_2$) is used. SERS (Figure 3f) of nanoparticles obtained from the Sn−acac reaction shows five peaks and are assigned to CZTS (290, 335, and 371 cm^{-1}), CTS (320 cm^{-1}), and ZnS (shoulder at 354 cm^{-1}). The nanoparticles obtained from the Sn−acac reaction give uniform squarelike nanoparticles (Figure 3e) with a narrower size distribution of 10 ± 3 nm and a mixture of wurtzite (CZTS) and stannite (CTS) crystal structures (Figure S5, Supporting Information). The decrease in the reactivity of Sn^{4+} slows the diffusion of Sn^{4+} into $Cu_{2-x}S$ nanoparticles thus affecting the rate of CTS nanoparticle formation. As established earlier, the growth route of the CZTS phase is highly specific. Since the formation of the CTS phase is an intermediate phase before the diffusion of Zn^{2+} occurs for formation of CZTS nanoparticles, the diffusion of Zn^{2+} ions into the CTS phase is slowed down too. A possible explanation for the presence of CZTS, CTS, and ZnS phases is the result of slowing down of Zn^{2+} ions consumption, leading to the reaction of thiol with excessive Zn^{2+} to form ZnS, possibly as a heterophase on $Cu_{2-x}S$/CTS nanoparticles.[41,42] The formation of ZnS deprives the reaction system with Zn^{2+} for the phase transformation from the CTS phase to the CZTS phase hence giving rise to CTS, CZTS, and ZnS phases.

Lastly, a stronger binding ligand−zinc complex ($Zn(acac)_2$) is used. SERS (Figure 3h) of nanoparticles obtained from the Zn−acac reaction shows three peaks at 292, 334, and 370 cm^{-1} indicating compositionally pure CZTS phase. CZTS nanoparticles obtained from Zn−acac (Figure 3g) show bricklike morphology with a size distribution of 9 ± 3 nm and pure wurtzite (CZTS) crystal structure (Figure S4, Supporting Information). The size distribution is much narrower as compared to the OAc reaction (Figure 3a), suggesting a more homogeneous nanoparticle growth with reduced Zn cation reactivity, while at the same time producing compositional pure CZTS phase. The observation of compositionally pure CZTS is unexpected from the Zn−acac reaction. The reduced Zn^{2+} reactivity is supposed to hinder the rate of Zn^{2+} diffusion into CTS to form the CZTS phase, and formation of CTS should be observed. The absence of the CTS phase is likely due to the affinity of Zn^{2+} for DDT and the small ionic radius of Zn^{2+} (74 pm).[50] Due to the small ionic radius, diffusion of Zn^{2+} into the growing CTS lattice is still highly favorable despite using a more stable chelating ligand, hence resulting in the formation of compositionally pure CZTS. It is shown here that the rate of formation of the CTS phase is crucial in ensuring pure CZTS phase formation and the need to balance the rate of all three growth steps to achieve pure CZTS phase is critical. These findings further prompt the need to establish the possible effect of thiol concentration on CZTS nanoparticle formation as the amount of sulfur (DDT) can influence the rate of phase formation.

Understanding the Influence of Thiol Concentration on CZTS Nanoparticle Formation.

In addition to the metal precursor reactivity, the influence of the amount of DDT present as a sulfur source in the reaction is studied. The amount of DDT is increased from 1 mL (used in all previous reactions above) to 5 mL and fixed for all the reactions. The SERS spectrum (Figure 4b) of nanoparticles obtained from the OAc reaction shows five peaks, which can be assigned to CZTS (290, 336, and 371 cm^{-1}), CTS (320 cm^{-1}), and ZnS (shoulder at 355 cm^{-1}). In addition, nanorods (Figure 4a) are observed
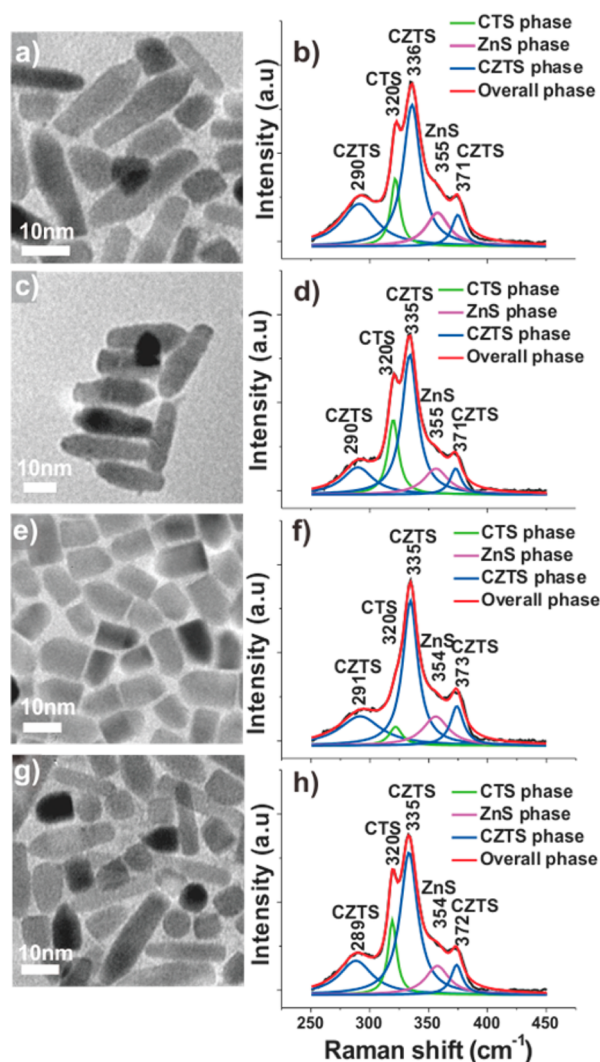

Figure 4. TEM images (left column) and SERS spectra (right column) of CZTS nanoparticles synthesized using different reaction setups at a 5 mL amount of DDT. (a, b) setup I, Oac; (c, d) setup II, Cu−acac; (e, f) setup III, Sn−acac; (g, h) setup IV, Zn−acac.

with a size distribution of 21 ± 5 nm with a mixture of wurtzite (CZTS) and stannite (CTS) crystal structures (Figure S2, Supporting Information). In comparison to 1 mL of DDT used previously (Figure 3b) that gives pure CZTS phase, using 5 mL DDT gives mixed phases. The same observation is noted for the Cu−acac and Zn−acac reactions, where both SERS spectra of the Cu−acac (Figure 4d) and Zn−acac (Figure 4h) reactions show five peaks and are assigned to CZTS (∼290, 335, and 371 cm^{-1}), CTS (∼320 cm^{-1}), and ZnS (shoulder at ∼355 cm^{-1}). Nanorods (Figure 4c, g) with a mixture of wurtzite (CZTS) and stannite (CTS) crystal structures are obtained as well (Figures S3 and S4, Supporting Information). The observation of a mixed compositional phase can be ascribed to mismatched reactivities leading to sequential phase segregation and nonuniform elemental distribution.[51]

On the other hand, when 5 mL of DDT is used in the Sn−acac reaction, the SERS spectrum (Figure 4f) shows a decrease in the CTS peak intensity (shoulder at 320 cm^{-1}) with respect to the CZTS peak (∼335 cm^{-1}). A small shoulder at ∼354 cm^{-1} indicates the presence of a small amount of ZnS phase. These two observations imply that less CTS and ZnS phases

are present than in the OAc, Cu−acac, and Zn−acac reactions. In addition bulletlike nanoparticles (Figure 4e) with mixed wurtzite (CZTS) and stannite (CTS) crystal structures (Figure S5, Supporting Information) are obtained with a size distribution of ∼20 ± 5 nm. This phenomenon is again in contrast with the Sn−acac reaction at 1 mL of DDT added, where the formation of CTS and ZnS are prominently observed. This opposing trend of phase formation with varying DDT concentrations (Figure S6, Supporting Information) suggests a nonzero reaction order with respect to sulfur ($d \neq 0$) in the formation of CZTS nanoparticles (Figure 5a).
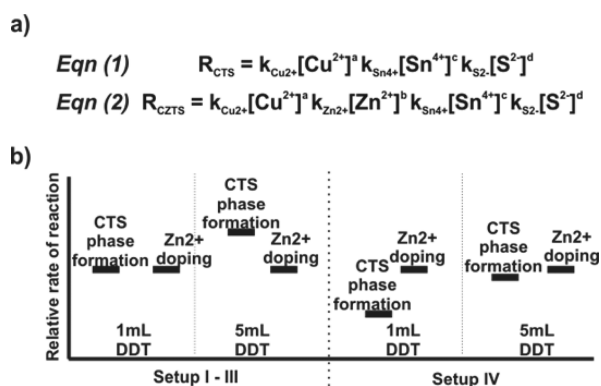

Figure 5. (a) Proposed equations for the rate of reaction of CTS and CZTS phases and (b) proposed relative rates of reaction for CTS formation and Zn^{2+} doping.

Two observations made suggest the purity of CZTS nanoparticles to be controlled by the relative rates of formation of CTS phase formation, and the rate of formation is highly dependent on the amount of DDT used. First, the observation of purer CZTS-phase nanoparticles obtained from the Sn−acac reaction with 5 mL of DDT as compared to 1 mL of DDT confirms that the rate of ZnS formation is not accelerated by increasing the amount of thiol source. This observation ruled out the formation of the ZnS phase observed in the OAc, Cu−acac, and Zn−acac reactions at 5 mL of DDT to be due to the increase in the rate of ZnS phase formation, which in turn deprives the reaction system with free Zn^{2+} cations to convert from the CTS to CZTS phase. Second, the observation of purer CZTS-phase nanoparticles obtained from the Sn−acac reaction compared to the nanoparticles obtained from the OAc, Cu−acac, and Zn−acac reactions at 5 mL of DDT and 5 mL of oleylamine (Oam) confirms that there is no ligand hindering effect arising from the high amount of DDT and Oam added. Therefore, we proposed that the purity of CZTS nanoparticles is controlled by the relative rates of formation of CTS and Zn^{2+} doping into CTS. The rate of CTS formation is accelerated in the presence of a large excess of sulfur source when the DDT volume is increased from 1 to 5 mL (Figures 3 and 4). As the rate of CTS formation increases, the diffusion rate of Zn^{2+} into the CTS matrix has to be comparable with the rate of CTS phase formation to completely transform the CTS phase into the CZTS phase. The fact that both CTS and ZnS phases are observed (Figure 4b, d, h) suggests that the diffusion rate of Zn^{2+} is slower than the rate of CTS phase formation, leaving the unreacted Zn^{2+} to react with DDT to form the ZnS phase for the OAc, Cu−acac, and Zn−acac reactions. On the other hand, when 5 mL of DDT is used in the Sn−acac reaction, the SERS spectra (Figure 4f) show a decrease in CTS peak

intensity (shoulder at 320 cm^{-1}) with respect to the CZTS peak (∼336 cm^{-1}). A small shoulder at ∼354 cm^{-1} indicates the presence of a small amount of the ZnS phase. This phenomenon at 5 mL of DDT can be ascribed to the increased rate of CTS phase formation to a level comparable to Zn^{2+} doping leading to the formation of the CZTS phase. The presence of a shoulder at 320 cm^{-1} (CTS phase) indicates that even at 5 mL of DDT, the rate of CTS phase formation is still slower than the Zn^{2+} diffusion process and the formation of the ZnS phase (shoulder at 354 cm^{-1}) inhibits the complete conversion of CTS to CZTS.

To summarize the mechanism of CZTS nanoparticle formation, the proposed relative reaction rates are shown in Figure 5b. For the OAc, Cu−acac, and Zn−acac reactions at 1 mL of DDT, the relative rates of CTS phase formation and Zn^{2+} doping are almost comparable and result in the formation of pure-phase CZTS. At 5 mL of DDT, the relative rate of CTS phase formation is much higher than Zn^{2+} doping resulting in incomplete CTS phase conversion and ZnS phase formation. On the other hand, due to the decrease in reactivity of Sn^{4+} in the Sn−acac reaction, at 1 mL of DDT, the relative rate of CTS phase formation is much lower than the OAc, Cu−acac, and Zn−acac reactions. Assuming the reactivity of Zn^{2+} doping remains unchanged and there are less CTS nanoparticles to react with, the excess Zn^{2+} ions react with DDT to form the ZnS phase. By increasing the DDT volume to 5 mL, the rate of CTS phase formation increases hence providing more CTS phase for Zn^{2+} doping to take place. This phenomenon results in purer CZTS-phase nanoparticles that is seen from Figures 4h and 5h for the Sn−acac reaction. Therefore, on the basis of the observation of the Sn−acac reaction, the preferential formation of the CZTS phase over the CTS phase is highly dependent on the rate of CTS phase formation for a comparable rate of Zn^{2+} doping into the crystal lattice.

Understanding the Influence of TOPO Ligand on Elemental Composition. In addition to the ability to control the formation of single-phase CZTS nanoparticles, the elemental composition of CZTS nanoparticles has to be optimize as it has been shown to influence the efficiency of device performance significantly.[8] By using energy-dispersive X-ray (EDX) characterization, it is observed that all as-synthesized nanoparticles (Figure S7, Supporting Information) show a common trend of having compositionally Zn poor ((Zn/Sn) ∼ 0.5−0.7) at low DDT amount and higher Zn content ((Zn/Sn) ∼ 0.8−1.0) at higher DDT amount for all reaction setups (Figure S8, Supporting Information). It is noted that the Zn−acac reaction setup that gives the purest CZTS phase at 1 mL of DDT (Figure 6a) is Zn poor, which is not ideal for thin-film fabrication. Further study to optimize the elemental composition is carried out by adjusting the concentration of trioctylphosphine oxide (TOPO) amount based on the molar ratio of TOPO to the cations (Figure 6a). Initially, following the work of Singh et al.,[22] 1.5× TOPO is used for all reaction setups. It is observed that, by lowering the TOPO amount, we are able to get higher Zn content (Figure 6a) while maintaining CZTS-phase purity as shown in Figure 6b. It is found that, at 0.75× TOPO, we are able to get the highest consistency and lowest error margin of less than ±5% from SERS and energy-dispersive spectroscopy (EDS) characterization. It can be understood that TOPO is essential for achieving high reproducibility and at the same time affecting the amount of Zn incorporating into the nanoparticles. The elemental composition (Figure 6a) of nanoparticles obtained from the
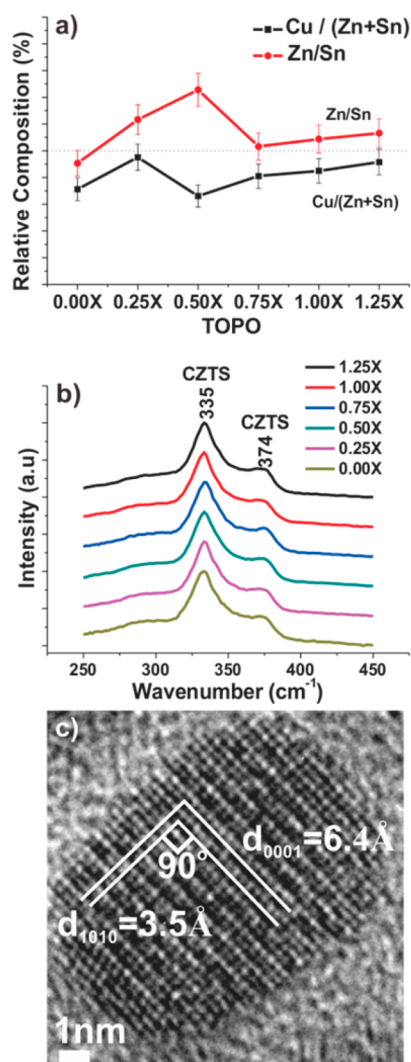
Figure 6. (a) Zn−acac with varying TOPO mole ratios at 1 mL of DDT. (b) SERS of CZTS nanoparticles (Zn−acac) at varying TOPO mole ratios. (c) HRTEM image of a CZTS nanoparticle (Zn−acac) at 0.75× TOPO.

Zn−acac reaction with 1 mL of DDT is optimized to near stoichiometry ratio of copper poor (Cu/Sn+Zn) = 0.9 ± 0.1 and zinc rich (Zn/Sn) = 1.1 ± 0.1 that was reported to yield high CZTS device efficiency.[8] From the high-resolution TEM (HRTEM) image (Figure 6c) of optimized CZTS nanoparticles, a lattice constant of 6.4 Å is indexed to the (0001) plane and a lattice constant of 3.5 Å is indexed to the (1010) plane 90° to the (0001) plane. The growth along the (002) plane is in agreement with a previous report on the selective growth of wurtzite crystal along the c axis.[22,52] In addition, X-ray photoelectron spectroscopy (XPS) measurement (Figure S9, Supporting Information) of CZTS nanoparticles showed distinctive peaks at 931.22 and 951.06 eV corresponding to Cu^+, 1047.52 and 1043.2 eV corresponding to Zn^{2+}, 485.6 and 489.12 eV corresponding to Sn^{4+}, and 161.76 and 162.60 eV corresponding to S^{2-}. This XPS data confirms that the oxidation numbers of the elements (i.e., Cu^+, Zn^{2+}, Sn^{4+}, S^{2-}) of the final product agrees with the expected values corresponding to the CZTS quaternary system.

CONCLUSIONS

SERS is used for the first time as a sensitive tool for material phase characterization, allowing us to monitor the growth mechanism of CZTS nanoparticles to proceed via three growth steps. It is found that the formation of CZTS proceeds via nucleation of $Cu_{2-x}S$ nanoparticles followed by diffusion of Sn^{4+} into $Cu_{2-x}S$ nanoparticles to form kinetically driven CTS nanoparticles and lastly diffusion of Zn^{2+} into CTS nanoparticles to form CZTS nanoparticles. The most crucial growth step to ensure a pure CZTS phase has been revealed to be the growth of the intermediate CTS phase. The selective CZTS phase formation over the CTS phase has been shown by carefully maintaining the rate of CTS phase formation to be similar to the rate of Zn^{2+} ion diffusion via controlling the coordinating strengths of the chelating ligands of metal precursors. It is also found that CTS formation is very sensitive to the reactivity of Sn precursor and the amount of sulfur source. After a systematic study, the most optimized reaction condition to form pure CZTS nanoparticles is found to be at low DDT volume of 1 mL and using $Cu(Oac)_2$, $Zn(acac)_2$, and $Sn(oac)_4$ as the metal precursors. Not only can this study serves as a platform to explain the formation of other CMTS (i.e., M = Co^{2+}, Ni^{2+}, Mn^{2+}, Fe^{2+}) nanoparticles, this ability of producing pure-phase CZTS nanoparticles holds the potential to achieve higher solar cell efficiency and even enabling large-scale production of devices.

METHODS

Chemicals and Materials. Copper(II) acetate monohydrate ($Cu(OAc)_2 \cdot H_2O$, Aldrich, >98%), copper(II) acetylacetonate (Cu-$(acac)_2$, Aldrich, 97%), zinc acetate dihydrate ($Zn(OAc)_2 \cdot 2H_2O$, Aldrich, >98%), zinc acetylacetonate ($Zn(acac)_2$, Aldrich, 97%), tin(IV) bis(acetylacetonate) dichloride ($Sn(acac)_2Cl_2$, Adrich, 98%), tin(IV) acetate ($Sn(OAc)_4$, Aldrich), trioctylphosphine oxide (TOPO, Aldrich, 90%), 1-octadecene (ODE, Aldrich, 90%), 1-dodecanethiol (DDT, Aldrich, 98%), and oleylamine (OAm, Acros, 97%) were used without further purification.

Synthesis of CZTS Nanoparticles. In a typical reaction, stoichiometric amounts of 0.442 mmol of $Cu(OAc)_2$, 0.234 mmol of $Zn(OAc)_2$, and 0.221 mmol of $Sn(OAc)_4$ were added into a 50 mL three-neck round-bottom flask containing 10 mL of ODE and TOPO (1.37 mmol). A 1−5 mL volume of DDT and 1−5 mL of Oam (DDT/Oam, 1:1) were injected at 150 °C and heated to 240 °C. During the heating process, reaction mixtures were allowed to react for 90 min once the temperature exceeded 200 °C. After 90 min, the solution was cooled naturally to room temperature by removing the reaction flask from the heating mantle. A 2 mL volume of toluene was added to quench the reaction at 80 °C as discussed by Singh et al.[22] CZTS nanoparticles were then washed with 1% v/v dodecanethiol/hexane and ethanol in a ratio of 1:5 and centrifuged twice at 7500 rpm for 3 min to separate the excess ligands from the CZTS nanoparticles. The nanoparticles were collected and dried in a N_2 box before storage. Dried nanoparticles can be dispersed in either hexane/chloroform or toluene.

Characterization. For scanning electron microscopy−energy dispersive spectroscopy (SEM-EDS), a concentrated CZTS nanoparticle solution in hexane was drop-cast (1 mL, 40 mg/mL) onto a Si/SiO$_x$ substrate (10 mm × 10 mm) and allowed to dry into a flat film in an enclosed Petri dish. The film was ensured to be thick enough so that no Si signal was picked up. The film was analyzed within the day after drying at ambient condition using a JEOL-JSM-7600F scanning electron microscope at 30 keV/8 mA for 10 min/spot at 5K magnification. The final elemental composition was calculated by averaging a total of nine spots (50 × 50 μm/spot). When the error margin is above 20%, the samples were prepared again and reanalyzed. TEM images were obtained using a JEOL-JEM-1400 electron

6690

dx.doi.org/10.1021/ja501786s | *J. Am. Chem. Soc.* 2014, 136, 6684−6692

microscope at an accelerating voltage of 100 kV. HRTEM images were obtained using a JEOL-JEM-2010 electron microscope at an accelerating voltage of 200 kV. XRD patterns were obtained using a Bruker D8 Advance with Cu Kα radiation (1.5406 Å) at 0.02°/s scan rate, 2 s accumulation time, and in 2θ ranging from 20° to 70° and analyzed using Topas. A 50 nm thick Au film on Si was prepared using thermal evaporation to serve as a substrate for SERS measurements. The thickness of the Au film was monitored by quartz crystal microbalance, and the deposition rate was 0.5 Å/s. A diluted CZTS nanoparticle solution in hexane was then drop-casted (20 μL, 4 mg/mL) onto a Au-coated Si wafer (5 mm × 5 mm) to form a thin film (~10 ± 5 nm) for SERS measurements. Both Raman and SERS spectroscopies were performed using a Horiba JY LabRAM HR Raman system with an excitation wavelength of 632.5 nm (power = 0.95 mW) supplied by an argon laser. All mapping experiments were performed using a 100× objective lens (NA = 0.9) with 30 s accumulation time between 200 and 1000 cm^{-1} and stage movement of 5 μm steps.

■ ASSOCIATED CONTENT

Ⓢ Supporting Information

Additional TEM and SEM images, XRD, Rietveld refinements, crystal structure parameters, XPS, SERS spectra, and EDX measurements of as-synthesized CZTS nanoparticles. This material is available free of charge via the Internet at http://pubs.acs.org.

■ AUTHOR INFORMATION

Corresponding Authors
xyling@ntu.edu.sg
lydiawong@ntu.edu.sg

Notes
The authors declare no competing financial interest.

■ ACKNOWLEDGMENTS

■ REFERENCES

(1) Tanaka, K.; Oonuki, M.; Moritake, N.; Uchiki, H. *Sol. Energy Mater. Sol. Cells* **2009**, *93*, 583.

(2) Katagiri, H.; Jimbo, K.; Maw, W. S.; Oishi, K.; Yamazaki, M.; Araki, H.; Takeuchi, A. *Thin Solid Films* **2009**, *517*, 2455.

(3) Mitzi, D. B.; Gunawan, O.; Todorov, T. K.; Wang, K.; Guha, S. *Sol. Energy Mater. Sol. Cells* **2011**, *95*, 1421.

(4) Henry, C. H. *J. Appl. Phys.* **1980**, *51*, 4494.

(5) Wang, W.; Winkler, M. T.; Gunawan, O.; Gokmen, T.; Todorov, T. K.; Zhu, Y.; Mitzi, D. B. *Adv. Energy Mater.* [Online early access]. DOI: 10.1002/aenm.201301465. Published Online: Nov 27, **2013**. http://onlinelibrary.wiley.com/doi/10.1002/aenm.201301465/full.

(6) Polizzotti, A.; Repins, I. L.; Noufi, R.; Wei, S.-H.; Mitzi, D. B. *Energy Environ. Sci.* **2013**, *6*, 3171.

(7) Steinhagen, C.; Panthani, M. G.; Akhavan, V.; Goodfellow, B.; Koo, B.; Korgel, B. A. *J. Am. Chem. Soc.* **2009**, *131*, 12554.

(8) Guo, Q.; Ford, G. M.; Yang, W.-C.; Walker, B. C.; Stach, E. A.; Hillhouse, H. W.; Agrawal, R. *J. Am. Chem. Soc.* **2010**, *132*, 17384.

(9) Todorov, T. K.; Tang, J.; Bag, S.; Gunawan, O.; Gokmen, T.; Zhu, Y.; Mitzi, D. B. *Adv. Energy Mater.* **2013**, *3*, 34.

(10) Wang, K.; Gunawan, O.; Todorov, T.; Shin, B.; Chey, S. J.; Bojarczuk, N. A.; Mitzi, D.; Guha, S. *Appl. Phys. Lett.* **2010**, *97*, 143508.

(11) Repins, I.; Beall, C.; Vora, N.; DeHart, C.; Kuciauskas, D.; Dippo, P.; To, B.; Mann, J.; Hsu, W.-C.; Goodrich, A.; Noufi, R. *Sol. Energy Mater. Sol. Cells* **2012**, *101*, 154.

(12) Cheng, A. J.; Manno, M.; Khare, A.; Leighton, C.; Campbell, S. A.; Aydil, E. S. *J. Vac. Sci. Technol., A* **2011**, *29*, 051203.

(13) Guo, Q.; Hillhouse, H. W.; Agrawal, R. *J. Am. Chem. Soc.* **2009**, *131*, 11672.

(14) Chen, S.; Yang, J.-H.; Gong, X. G.; Walsh, A.; Wei, S.-H. *Phys. Rev. B* **2010**, *81*, 245204.

(15) Chen, S.; Gong, X. G.; Walsh, A.; Wei, S.-H. *Appl. Phys. Lett.* **2010**, *96*, 021902.

(16) Wagner, R.; Wiemhöfer, H. D. *J. Phys. Chem. Solids* **1983**, *44*, 801.

(17) Nozaki, H.; Shibata, K.; Ohhashi, N. *J. Solid State Chem.* **1991**, *91*, 306.

(18) Zhou, H.; Hsu, W.-C.; Duan, H.-S.; Bob, B.; Yang, W.; Song, T.-B.; Hsu, C.-J.; Yang, Y. *Energy Environ. Sci.* **2013**, *6*, 2822.

(19) Chesman, A. S. R.; Duffy, N. W.; Peacock, S.; Waddington, L.; Webster, N. A. S.; Jasieniak, J. J. *RSC Adv.* **2013**, *3*, 1017.

(20) Jiang, H.; Dai, P.; Feng, Z.; Fan, W.; Zhan, J. *J. Mater. Chem.* **2012**, *22*, 7502.

(21) Wang, J.-J.; Hu, J.-S.; Guo, Y.-G.; Wan, L.-J. *NPG Asia Mater.* **2012**, *4*, e2.

(22) Singh, A.; Geaney, H.; Laffir, F.; Ryan, K. M. *J. Am. Chem. Soc.* **2012**, *134*, 2910.

(23) Zhang, W.; Zhai, L.; He, N.; Zou, C.; Geng, X.; Cheng, L.; Dong, Y.; Huang, S. *Nanoscale* **2013**, *5*, 8114.

(24) Thompson, M. J.; Ruberu, T. P. A.; Blakeney, K. J.; Torres, K. V.; Dilsaver, P. S.; Vela, J. *J. Phys. Chem. Lett.* **2013**, *4*, 3918.

(25) Riha, S. C.; Parkinson, B. A.; Prieto, A. L. *J. Am. Chem. Soc.* **2011**, *133*, 15272.

(26) Kumar, P.; Gusain, M.; Nagarajan, R. *Inorg. Chem.* **2011**, *50*, 3065.

(27) Fernandes, P. A.; Salomé, P. M. P.; da Cunha, A. F. *J. Alloys Compd.* **2011**, *509*, 7600.

(28) Grossberg, M.; Krustok, J.; Raudoja, J.; Timmo, K.; Altosaar, M.; Raadik, T. *Thin Solid Films* **2011**, *519*, 7403.

(29) Vasilevskiy, M. I.; Trallero-Giner, C. *Phys. Status Solidi B* **2010**, *247*, 1488.

(30) Hollricher, O. In *Confocal Raman Microscopy*; Dieing, T., Hollricher, O., Toporski, J., Eds.; Springer: Berlin, Germany, 2011; Vol. *158*.

(31) Schwartzberg, A. M.; Zhang, J. Z. *J. Phys. Chem. C* **2008**, *112*, 10323.

(32) Kneipp, K.; Wang, Y.; Kneipp, H.; Perelman, L. T.; Itzkan, I.; Dasari, R. R.; Feld, M. S. *Phys. Rev. Lett.* **1997**, *78*, 1667.

(33) Giannini, V.; Fernández-Domínguez, A. I.; Heck, S. C.; Maier, S. A. *Chem. Rev.* **2011**, *111*, 3888.

(34) Kelly, K. L.; Coronado, E.; Zhao, L. L.; Schatz, G. C. *J. Phys. Chem. B* **2002**, *107*, 668.

(35) Cui, Y.; Deng, R.; Wang, G.; Pan, D. *J. Mater. Chem.* **2012**, *22*, 23136.

(36) Yu, Y.-M.; Hyun, M. H.; Nam, S.; Lee, D.; O, B.; Lee, K. S.; Yu, P. Y.; Choi, Y. D. *J. Appl. Phys.* **2002**, *91*, 9429.

(37) Liao, H.-C.; Jao, M.-H.; Shyue, J.-J.; Chen, Y.-F.; Su, W.-F. *J. Mater. Chem. A* **2013**, *1*, 337.

(38) Wang, S.; Huang, Q.; Wen, X.; Li, X.-y.; Yang, S. *Phys. Chem. Chem. Phys.* **2002**, *4*, 3425.

(39) Munce, C. G.; Parker, G. K.; Holt, S. A.; Hope, G. A. *Colloids Surf., A* **2007**, *295*, 152.

(40) Li, M.; Zhou, W.-H.; Guo, J.; Zhou, Y.-L.; Hou, Z.-L.; Jiao, J.; Zhou, Z.-J.; Du, Z.-L.; Wu, S.-X. *J. Phys. Chem. C* **2012**, *116*, 26507.

(41) Yi, L.; Tang, A.; Niu, M.; Han, W.; Hou, Y.; Gao, M. *CrystEngComm* **2010**, *12*, 4124.

(42) Han, S.-K.; Gong, M.; Yao, H.-B.; Wang, Z.-M.; Yu, S.-H. *Angew. Chem., Int. Ed.* **2012**, *51*, 6365.

(43) Sigel, H. *Angew. Chem., Int. Ed.* **1975**, *14*, 394.

(44) Pearson, R. G. *J. Am. Chem. Soc.* **1963**, *85*, 3533.

(45) Bard, A. J.; Parsons, R.; Jordan, J. *Standard Potentials in Aqueous Solution*; Taylor & Francis: New York, 1985.

(46) Liu, Y.; Yao, D.; Shen, L.; Zhang, H.; Zhang, X.; Yang, B. *J. Am. Chem. Soc.* **2012**, *134*, 7207.

(47) Bouroushian, M. *Electrochemistry of Metal Chalcogenides*; Springer: Berlin, Germany, 2010.

(48) Irving, H.; Williams, R. J. P. *J. Chem. Soc.* **1953**, 3192.

(49) Chattaraj, P. K.; Lee, H.; Parr, R. G. *J. Am. Chem. Soc.* **1991**, *113*, 1855.

(50) Shannon, R. *Acta Crystallogr., Sect. A: Found. Crystallogr.* **1976**, *32*, 751.

(51) Ruberu, T. P. A.; Albright, H. R.; Callis, B.; Ward, B.; Cisneros, J.; Fan, H.-J.; Vela, J. *ACS Nano* **2012**, *6*, 5348.

(52) Fan, F. J.; Wu, L.; Gong, M.; Chen, S. Y.; Liu, G. Y.; Yao, H. B.; Liang, H. W.; Wang, Y. X.; Yu, S. H. *Sci. Rep.* **2012**, *2*, 952.